Cryogenic scanning Hall-probe microscope with centimeter scan range and submicron resolution

Rafael B. Dinner, M. R. Beasley, and Kathryn A. Moler[a)]
Geballe Laboratory for Advanced Materials, Stanford University, Stanford, California 94305

(Received 28 June 2005; accepted 22 August 2005; published online 5 October 2005)

We have constructed a scanning Hall-probe microscope that combines a 1×4 cm scan range with 200 nm positioning resolution by coupling stepper motors to high-resolution drivers and reducing gears. The instrument is uniquely suited for efficient magnetic imaging of mesoscopic devices, media, and materials, operating from 4 K to room temperature with fast turn-around time. Its potential for studying dissipation in coated conductors—high-T_c superconducting tapes—is demonstrated via model systems. We image an entire sample of $YBa_2Cu_3O_{7-\delta}$, then zoom in to individual fluxons. Flux penetration into a single artificial grain boundary is imaged with 4×10^{-3} G/$\sqrt{\text{Hz}}$ field resolution and 25 μs time resolution by averaging over cycles of ac driving current. Using the resulting magnetic movie, we map out ac power losses. © *2005 American Institute of Physics.* [DOI: 10.1063/1.2072438]

I. INTRODUCTION

Scanning Hall-probe microscopy (SHPM) has many practical advantages among magnetic imaging techniques.[1,2] It offers submicron spatial resolution and milligauss field resolution. Scanning generally takes at least a second to acquire an image, but the inherent response time of Hall probes is much faster enabling repeatable phenomena to be imaged with microsecond time resolution as described in this article. For comparison, Lorentz microscopy[3] offers better than 10 nm spatial resolution and can generate hundreds of images per second but is limited to samples thin enough (70 nm) to be transparent to electrons. Magneto-optics[4] can also image at video rates but is inferior to SHPM in both spatial and field resolutions. Scanning superconducting quantum interference device (SQUID) microscopy[5] offers excellent field sensitivity but has not yet achieved submicron spatial resolution and has a more limited range of sensor operating temperature. Magnetic force microscopy (MFM)[6] offers better spatial resolution than SQUID or SHPM, but at a cost in magnetic sensitivity. MFM also applies a local field large enough to perturb the sample in some cases.

In SHPM, scanning has typically been accomplished with piezos, whose motion is limited and decreases at cryogenic temperatures. Work to amplify the motion of piezos resulted in a scan range of 275 μm at 4 K.[7] A similar range was obtained by maintaining a piezo-based scanning mechanism at room temperature while the sample is cooled.[8] On the other hand, SHPM has achieved a 5 mm scan range using motors and micrometer screws in place of piezos[9] In that case, however, the minimum pixel spacing was limited by the motors to 1.25 μm.

In the present work, we also use motor-driven micrometers but couple them to improved electronics and reducing gears to achieve resolution comparable to piezo-based Hall-probe scanners, and limited by the sensor rather than by the scanning mechanism. As a result, we can image magnetic fields over centimeters of a sample, identify smaller areas of interest, and zoom in to image those areas with submicron resolution.

Applications of this multiscale characterization include material inhomogeneities or phase segregation, artificially patterned magnetic media, and arrays of mesoscopic devices. Well-controlled, long-range motion is convenient whenever alignment to a sample feature is necessary and to maintain this alignment between room and cryogenic temperatures, compensating for thermal contraction. For instance, one could use the large scan range to align to nanopatterned circuits and image current flow. Among materials, coated conductors—high-T_c superconducting tapes—require multiscale characterization to sort out weak spots due a variety of phenomena ranging from mechanical defects on a millimeter scale down to the interaction of a few vortices on the submicron scale of the London penetration depth.[10] The results presented here are precursors to such a study.

Fast turn-around time for changing samples is another element of the instrument design that helps, in the example of coated conductors, to secure the microscope's role in the development of practical materials which are still evolving, leading to many variants. Finally, the system exploits the excellent field sensitivity, spatial resolution, and operating temperature range of micro-Hall sensors.

II. DESIGN

A. Overview and example

A sketch of the system is shown in Fig. 1(a). We have adapted a Desert Cryogenics tabletop cryogenic probe station[11] normally used for manually positioning electrical probes on a cooled sample. In our instrument, a computer-controlled positioning stage rasters a Hall sensor over the sample surface. Measurements of the sensor's Hall resistance at a grid of positions on the surface are reconstructed into

[a)]Author to whom correspondence should be addressed; electronic mail: kmoler@stanford.edu

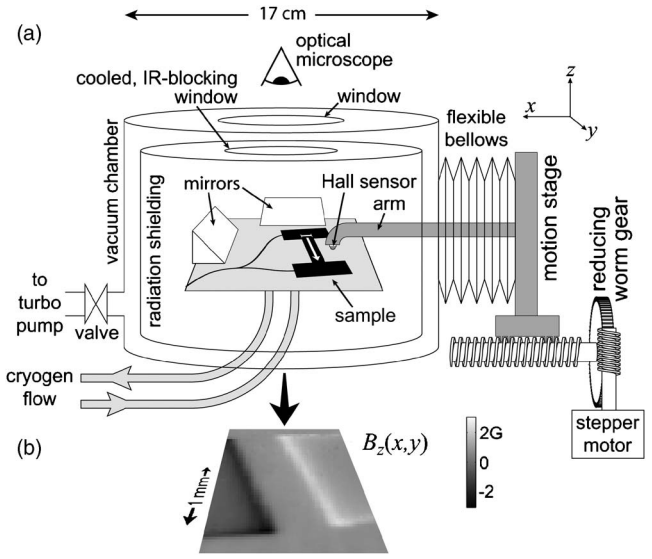

FIG. 1. (a) Sketch of the large area scanning Hall-probe microscope. A flow cryostat cools the sample. A Hall sensor is rastered over the sample surface. The sensor position is controlled by an external, stepper motor-based stage. The cryostat allows optical access from above and, via mirrors, from the sides. (b) Magnetic image of a millimeter long YBCO strip carrying 100 mA. This image uses only a fraction of the instrument's centimeter scan range.

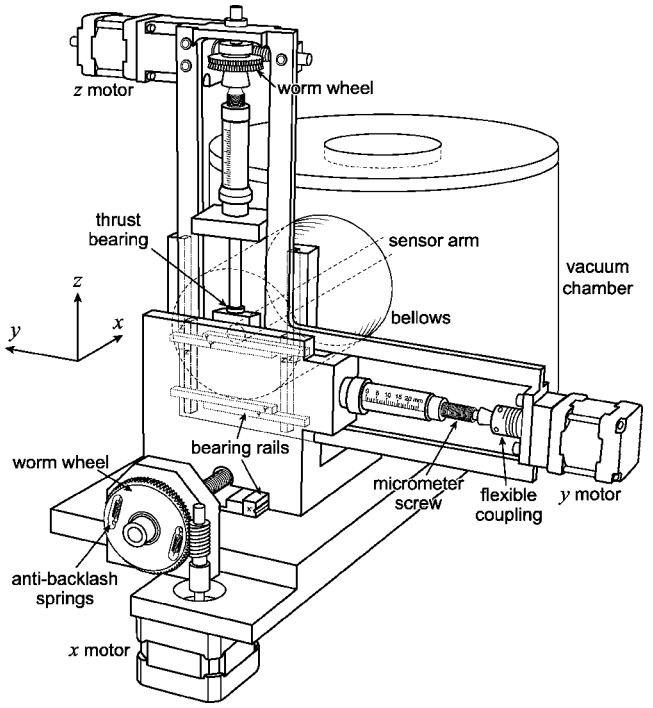

FIG. 2. Sketch of the three-axis stage that moves the sensor arm. Stepper motors drive micrometer screws to generate linear motion. For the x and z axes, worm gears first reduce the motors' rotation; for the y axis, the motor is coupled directly to the micrometer screw.

$B_z(x,y)$, an image of the vertical component of the local magnetic induction. The positioning stage is outside the cryostat; its motion is fed through to the vacuum chamber via flexible bellows. For further discussion of this design choice, see Sec. V C.

Figure 1(b) is a magnetic image of the sample depicted in Fig. 1(a). A film of the high-T_c superconductor $YBa_2Cu_3O_{7-\delta}$ (YBCO) is patterned into a bridge approximately 600 μm long by 150 μm wide and 300 nm thick. The entire structure occupies only a small portion of the instrument's 1×4 cm scan range.

The bridge is imaged at 50 K. At each pixel, dc currents of +100 and −100 mA are applied, and the corresponding magnetic fields are measured. Half the difference between the fields is scaled according to the color scale shown and plotted for each point. Retaining only the difference between the two fields measured reduces the effects of time variation in the sensor and any background field. A similar technique is described in more detail in Sec. IV C.

The applied currents are well below the expected critical current (3 A), and the superconductor displays the Meissner effect, with most of the current flowing along its edges. A line cut across the strip taken from the magnetic image is well modeled by accounting for thin film demagnetization effects and ignoring the strip's finite length.[12] The ease of aligning to and acquiring such a cut across the center of the bridge demonstrate this instrument's advantages over previous designs.

B. Stepper motor-based linear motion

The instrument's scan range and resolution result from a custom three-axis linear motion stage, shown in Fig. 2. We modified the manually manipulable stage included with the Desert Cryogenics probe station, coupling its micrometer screws to stepper motors. The pieces slide via rails that ride on crossed roller bearings. The motors are from Oriental Motor Co.'s VEXTA CFK II series, chosen for their high resolution and small size. The z and y axes each use a model PMM33BH2 motor, and the x axis uses a PK543NBWA. Each motor is powered by a model DFC5107T driver and takes 500 full steps per revolution of its shaft. The driver is capable of microstepping (holding the motor at positions between steps) with a nominal minimum increment of 1/250 full steps, though we have not characterized the accuracy of microstepping down to this resolution.

For the x axis, a 2 mm pitch screw is attached to the base of the cryostat by thrust bearings and mates to a Delrin nut on the stage, driving the stage along its rails as the screw turns in place. An 80-tooth worm gear with incorporated antibacklash springs is clamped to the end of the screw and is turned by a double-thread worm attached to a motor reducing the motor's movement by a factor of 40. As a result, the stage is expected to move 100 nm per step, with a nominal minimum microstep of 0.4 nm. The full range of the x stage is 5 cm.

The y stage is attached via rails to the x stage and driven by a 0.5 mm pitch screw. A motor shaft is attached directly to one end of this screw via a flexible coupling meant to convey rotations but reduce radial force. The stage moves 1 μm per full step, 4 nm per microstep. The y range is limited to about 1 cm by the large force need to stretch the bellows when the stage moves off center. This force creates friction in the micrometer and the stage that must be overcome by the motor.

All scans are rastered with scan lines in the y direction, from bottom to top, each line followed by retracting to the bottom y position and moving one increment along the x

axis, from left to right. Having no gear reduction on the y axis makes it capable of moving at 20 mm/s, though we typically operate at one-tenth of that speed. Even for a scan with a large pixel spacing such as 10 μm, the time taken in moving between pixels is smaller than the time taken in measuring at each pixel, typically 0.1–0.5 s. Thus a 200 $\times$200 pixel scan would take several hours and take only slightly longer with increasing pixel spacing.

The z stage couples to the y stage and shares most of its features but inserts a 60-tooth, double-thread, antibacklash worm gear between the motor and screw, reducing the step size to 33 nm per full step, 0.13 nm per microstep. The z motion is limited above by the arm hitting the top of the port in the radiation shield and below by the sensor hitting the sample stage, resulting in a range of 7 mm. Finally, the sensor arm bolts to the z stage. The position of each pixel in the images below is calculated from the number of steps input to the x and y stepper motors; we have not attempted to correct for position-dependent tilting of the arm or other factors that might (and probably do, as described in Sec. III B) prevent the sensor from moving exactly as predicted from the step size and gearing.

Combining the high resolution of the stepper motors and the reducing gears, the minimum step sizes for all axes are in the nanometer range. However, the sensor movement shows backlash of several microns probably reflecting some rotational play in the stage amplified by the length of the sensor arm. We deal with backlash by always approaching from one direction ($-x$,$-y$, and $+z$) and find good unidirectional repeatability, as quantified in Sec. III B.

C. Micro-Hall sensor fabrication and performance

Our magnetic sensor exploits the Hall effect in which applying current between two opposing leads of a conducting cross and measuring voltage across the other pair of opposing leads yield a Hall resistance that is proportional to the component of the magnetic field perpendicular to the leads averaged over the "sensitive area"—the intersection of the leads.[13] The sensor is fabricated from a high-mobility two-dimensional electron gas (2DEG) in a GaAs–$Al_{0.3}Ga_{0.7}As$ heterostructure with low carrier density for a large Hall resistance. The Hall cross is patterned with e-beam lithography and ion milling through the 2DEG donor layer creating four trenches to separate four leads, seen in Fig. 3(e).[14]

For the sensor used in Sec. III, the sensitive area is lithographically defined to be a square 500 nm on each side. A metal shield (90 nm of gold on 10 nm of titanium) is deposited over the entire tip extending back 260 μm. This shield is grounded to screen the sensor from electric fields. For the sensor in Sec. IV, the sensitive area is 700 nm on each side, and there is no shield. For both sensors, we verified that the Hall resistance is a linear function of the applied magnetic field for fields up to 0.5 T. We also calibrated, as a function of temperature from 2.5 to 320 K, the linear slope (Hall coefficient) and offset relating resistance to field for each sensor. The Hall coefficient is about 0.1 Ω/G below 100 K.

The zero-field offset in the Hall resistance, however, varies between cooldowns presumably due to electronic reconfigurations that change the effective geometry of the Hall

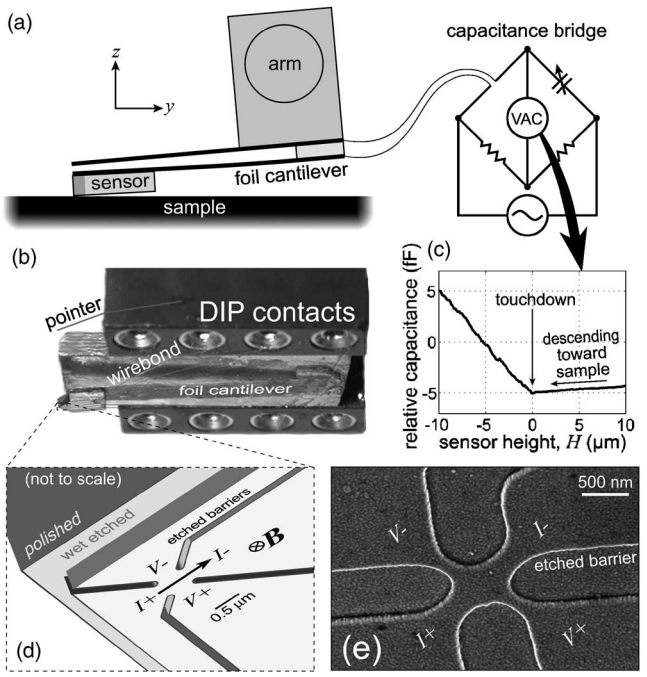

FIG. 3. (a) Sketch of the Hall sensor mounted on a foil cantilever that, together with a fixed metal plate above it, acts as a capacitor used to sense touchdown of the sensor on the sample. (b) Photo of the same, tilted to reveal the bottom of the assembly, which faces the sample. (c) Capacitance vs sensor height H above the sample surface indicates when the sensor has touched down. For $H<0$, capacitance abruptly starts to increase with decreasing sensor arm height. $H=0$ is defined by this measurement with 30 nm standard deviation. (d) Sketch showing the sensitive area (Hall cross) and its placement near a corner, defined by photolithography and wet etching that creates a step several microns deep followed by manual polishing to remove most of the remaining material. As in (b), the viewpoint is tilted to reveal the sensor's bottom face. (e) Scanning electron micrograph (SEM) of the Hall cross tilted 45° as in (d). For this sensor, similar to that used in Sec. III, the area is covered by a layer of gold to screen electric fields.

cross. It also exhibits switching noise which translates into B noise of up to 5 G. The noise has a $1/f$-like spectrum that intersects the white noise floor near 100 Hz, thus it can be eliminated along with the offset by measuring only fast changes in B (e.g., produced by an ac sample current). When it is necessary to measure a dc field, the offset is taken as a free, rather than calibrated, parameter. In the ac configuration at 400 Hz, with the sensor at 28 K, the measured field noise is 4×10^{-3} G/$\sqrt{\text{Hz}}$, mainly due to Johnson noise plus voltage noise added by the preamplifier. The measurement electronics varies between experiments and will be specified for each.

D. Sensor-sample alignment

A charge-coupled device (CCD) camera attached to a microscope looks directly down at the sample stage. It can zoom out to an area of 6.6×5.0 mm^2 or zoom in for a 3 μm resolution. To determine the sensor's height H relative to the sample, the two are viewed from the side via mirror wedges with angles slightly greater than 45°, as shown in Fig. 1(a).

The measurement of H is refined by touching the sensor to the surface at several points and recording the z positions at which the sensor touches down, as measured by a capacitive touchdown cantilever, illustrated in Figs. 3(a) and 3(b).

The sensor is mounted on a copper foil cantilever (approximately 10 mm long, 4 mm wide, and 20 μm thick), one end of which is attached to a copper plate but electrically isolated by a piece of glass. The cantilever and plate are separated by $\sim$100 μm forming a capacitor that allows one to detect when the Hall sensor is touching the sample: As the stepper motor stage lowers, the sensor corner near the Hall cross touches the surface first. Upon further lowering, the sensor and cantilever are deflected toward the plate increasing the capacitance, as in Fig. 3(c). Prior to touching down, the sensor appears to be slightly attracted to the surface, presumably due to an electrostatic interaction, causing the cantilever to deflect downward and the capacitance to decrease as H decreases. Touchdown is presumed to occur at the change in the slope of the capacitance versus H.

The change in slope can be identified by eye, but we also use an algorithm to automatically detect several points in succession with systematically higher capacitance than predicted by a linear fit to the preceding points. Then, via linear fits to the points before and after touchdown, we determine the touchdown location with a typical uncertainty of 30 nm. In this way, we find the sample surface, using optical alignment followed by capacitive touchdown, in a couple of minutes.

By determining the sample height at several locations, we approximate the plane of the surface. For larger scans where micron resolution is not necessary, the sensor is lifted at least several microns away from the surface and the height is adjusted at each step to maintain this distance from the known sample plane. To obtain higher-resolution images, however, we must minimize the height of the Hall cross above the sample. To this end, the arm descends 10 μm below the position at which the sensor first touches the sample then holds the z position fixed for each scan line, lifting above the sample plane between lines and descending again at the start of each line. The extra 10 μm causes the cantilever to apply a small downward force ensuring that the sensor corner remains in contact with the sample throughout each line. This "contact mode" wears down the sensor [as visible in scanning electron micrographs (SEMs), not shown] over several hundred two-dimensional scans (several meters of linear movement), but this rate is sufficiently gradual that we do not take any precautionary measures against it (such as coating the sensor with a protective layer).

In contact mode, the height of the sensitive area above the sample surface increases with the tilt of the sensor and is proportional to the distance from the sensitive area to the corner that touches the sample, as discussed quantitatively in Sec. III B. Photolithographic patterning, followed by wet etching to remove several microns of material, defines the corner closest to the cross as shown in Fig. 3(d). The part of the substrate that protrudes past the etched edges is then manually polished to within 20 μm of the edges so as not to interfere with the corner touching the sample.

The sensor tilt is measured optically by viewing the sensor via the mirror wedges. Tilt about the x axis is manually adjustable over a 10° range via a rotating connection between the arm and the motion stage even when the cryostat is evacuated and cooled. The y tilt is adjustable via the connection between the end of the arm and the dual inline pin (DIP) socket only when the cryostat is open.

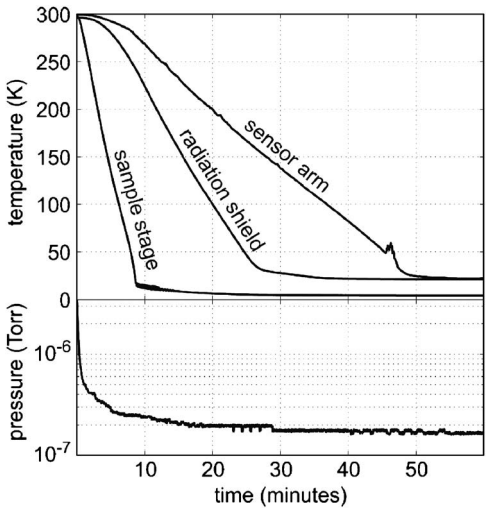

FIG. 4. Temperatures and pressure after insertion of the precooled liquid-helium transfer line into the cryostat. The sample stage cools from room temperature to near its final temperature of 4 K in less than 10 min. Other parts of the cryostat take longer to equilibrate.

Optical access to the sample stage from above is also useful for positioning the Hall sensor near a sample feature in x and y. However, when the sensor is directly over a feature, the feature is obscured. Instead, a small segment of wire (12 μm in diameter and several mm long) attached to the side of the DIP socket on which the sensor is mounted serves as a pointer, labeled in Fig. 3(b), and the relative x and y distances between the pointer tip and the sensor active area have been calibrated to within 20 μm. Between optical alignment and capacitive touchdown sensing, we can align to sample features in all three dimensions in a matter of a few minutes.

E. Cryogenic design and performance

Liquid helium or liquid nitrogen flows from a transfer dewar into the cryostat and through a high-impedance heat exchanger that cools the 5.4×5.4 cm^2 copper sample stage. The cryogen then flows through a second heat exchanger connected to the surrounding radiation shield with cooled infrared-blocking window. The sample stage and radiation shield are enclosed in a vacuum chamber with a second window. Before cooling, the chamber is evacuated for at least an hour by a turbo pumping system to below 10^{-5} Torr. Within the first minute of cooling, the system cryopumps to the 10^{-7} Torr range at which point the pump is typically valved off and powered down to reduce vibrational and electrical noise.

Figure 4 logs a cooldown using liquid helium. The base temperature of the sample stage, as read by a calibrated silicon diode thermometer heat sunk to one corner, is 4.20 K, or 3.52 K when pumping on the vapor outlet.[15] The radiation shield temperature, determined by a calibrated Cernox thermometer, reaches a minimum of around 20 K, varying with the helium flow rate. With its small thermal mass, the sample stage cools from room temperature to 4 K in less than 10 min

consuming only a couple of liters of helium. Operation requires about a liter per hour thereafter. Temperature control of the sample stage from 4 to 300 K with 5 mK stability is achieved with a 50 Ω, 50 W maximum resistive heater and by restricting the cryogen flow with a manual valve integrated into the transfer line.

Warming the cryostat from 4 K to room temperature takes several hours under vacuum with the sample stage heater set (conservatively) to output a few watts. Thus the total turn-around time for switching samples is at least four hours: After warming, unloading and loading samples takes only a few minutes, but the cryostat must then be evacuated for an hour and cooled again.

1. Sample heat sinking

With the sample and its electrical leads in vacuum, rather than liquid or vapor, and the short distances afforded by the compact flow cryostat, heat sinking is more challenging than in a traditional dewar. Eight electrical leads run from feedthroughs in the room-temperature vacuum chamber to the sample. Four of the leads are 0.13-mm-diameter Manganin resistance wires with a resistance of 50 Ω each at low temperature, maintaining a high thermal resistance between room temperature and the sample. These are not suitable, however, for carrying the ampere-level currents necessary for superconducting transport studies. So the other four leads are 0.10-mm-diameter copper with resistances of 0.3 Ω at low temperature. All leads are heat sunk to the radiation shield and then to the sample stage. The Manganin leads share one pair of heatsinks; the copper leads another. Each heat sink is made by wrapping and varnishing 10 cm of the wire around a copper bobbin which is bolted to the stage or radiation shield. In addition, 10 cm of the wire separate each connection from vacuum feedthrough to radiation shield to sample stage. The sample end of each lead terminates in a pin-and-socket connection to 4 cm of 0.10-mm-diameter copper wire which is soldered to a gold pad on a beryllium oxide heat sink chip varnished to the sample chuck. A 25-μm-diameter aluminum wire bond (or several for leads that will carry more than 200 mA) connects each pad to a gold pad deposited on the sample. The sample substrate is also varnished to the sample chuck, and most of the sample cooling flows through the substrate rather than the wires.

As a calibration of sample temperature, we use the superconducting transition of a thin film of niobium deposited on a 400-μm-thick oxidized silicon substrate, measured independently to be 8.73 K. In the scanner cryostat, as measured with the sample stage thermometer, the film shows a superconducting transition at 8.47 K in a four-point resistance measurement with Manganin leads and 5.39 K in a two-point configuration with copper leads. YBCO transition temperatures are also found to be within a few degrees of their expected values even with copper leads. Thus we expect that the actual sample temperature is a fraction of a degree higher than the thermometer temperature for high resistance leads and several degrees higher where it is necessary to use low resistance current leads.

2. Sensor heat sinking

The sensor arm is made of fiberglass and surrounded by a copper sheath that is heat sunk to the radiation shield. At the end of the arm inside the cryostat is a copper section cooled via a 1.6-mm-diameter copper braid sunk to the sample stage. For temperature control independent of the sample stage, the end of the sensor arm contains a 100 Ω platinum resistive thermometer using a standard calibration curve (i.e., not individually calibrated) and a 200 Ω, 12.5 W maximum heater. Figure 4 shows that the copper braid couples the arm and sample stage relatively weakly; the arm cooling rate is slower and the base temperature is about 15 degrees higher. This isolation is convenient for maintaining a constant arm temperature while changing the sample temperature but is not necessary for the measurements below.

The leads of the Hall sensor start from the room-temperature cryostat feedthroughs with 15 cm of ultraminiature coaxial cable consisting of a 0.20-mm-diameter copper center conductor and stainless-steel braided shield insulated by Teflon. These are soldered to 10 cm of the 0.13-mm-diameter phosphor-bronze wire that is varnished onto the temperature-controlled copper section of the arm. Finally, 8 cm of the 0.26-mm-diameter copper wire is soldered to each lead, wrapped and varnished onto the copper arm section, and terminates at a DIP socket from which the sensor assembly hangs facing down toward the sample. Cooling of the sensor occurs primarily through the leads, so the 8 cm sections of copper wires serve to reduce the time constant for equilibration and to help remove the heat generated in the sensor itself. Comparison of the sensor resistance to the arm thermometer during cooling and warming indicates that the sensor follows the thermometer with a characteristic lag of less then 5 min.

F. Vibration

Vibration of the sensor relative to the sample can blur or introduce artifacts into a scanned probe image. Our instrument is not specifically designed to minimize vibrations. It is isolated by rubber feet from an ordinary laboratory bench on a basement floor. The sensor hangs from a floppy cantilever attached to a long arm. However, for high-resolution images, the sensor touches the sample, coupling the two via static friction. The field is measured only when the sensor is held fixed at each pixel. We quantified vibrations in this configuration as follows.

We scan to find a position with a high magnetic field gradient[16] that will translate sensor movement into measurable field variation and hold the sensor at that position, applying a dc Hall current. The Hall voltage time trace is then recorded at 20 kilosamples/s for 50 s. For comparison, a time trace is recorded with the sensor retracted several hundred microns from the sample, where the gradient is much smaller. We find a statistically significant increase in noise at the position of high gradient. This extra noise is consistent with the 30 nm rms movement in x, 40 nm rms movement in y, or 60 nm rms movement in z. The actual movement is probably a combination of smaller movements along multiple axes. The blurring effect that such movement might

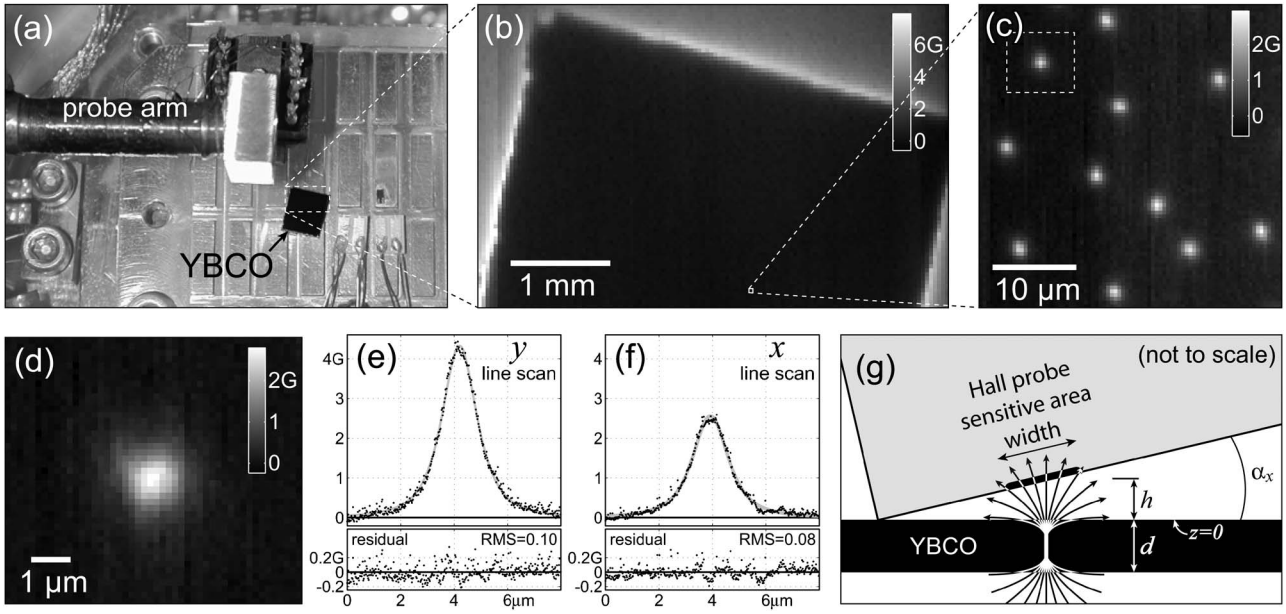

FIG. 5. (a) Top view photograph of a square section of a thin film of YBCO varnished to the sample stage. (b)–(d) Magnetic images of the square at several length scales, from its full width down to submicron resolution. Each white dashed box in (a)–(c) indicates the area scanned in the succeeding image. The pixel spacing in (d) is 200 nm. (e)–(f) After more careful sensor alignment, single rows of points near a vortex were scanned along the y, then x directions. These data (black points) were fitted (gray lines) with a model of the vortex field, depicted in (g).

cause, however, is still 20 times smaller than that caused by the Hall probe, as quantified in Sec. III.

III. DETERMINING RESOLUTION WITH VORTEX IMAGES

We use an Abrikosov vortex in a high-T_c superconducting film to calibrate the mechanical performance of our instrument. A vortex is a spatially sharp magnetic object whose field is well modeled.[17–19] Our sample is a film of YBCO, a well-studied material.[20]

A. Experimental configuration and data

A 5×5 mm^2 square piece of YBCO is varnished to the sample stage as shown in Fig. 5(a). The film consists of a 300 nm YBCO layer grown by pulsed laser deposition on top of a 30 nm CeO_2 buffer layer on a 400-μm-thick single-crystal $LaAlO_3$ (LAO) substrate. Another piece of the same film superconducts below 88 K (as determined by the maximum slope in the resistance versus temperature, with a transition width of 1 K). The sample is cooled in the laboratory's ambient field of about an oersted; the cryostat has no magnetic shielding. The sensor temperature is controlled at 30 K, and the sample temperature is uncontrolled ranging from 11.9 to 12.3 K.

After cooling, a field with a positive component of several oersteds in the vertical direction is applied by placing a permanent magnet on top of the cryostat. The area indicated by the white dashed rectangle in Fig. 5(a) is then scanned moving the sensor in a plane 40 μm above and parallel to the sample surface. A 146 Hz, 24 μA rms current is applied to the sensor and the in-phase component of the Hall voltage is measured with a lock-in amplifier.

The resultant image is shown in Fig. 5(b). The sample generates screening currents in response to the applied field enhancing the field just outside its edges. The small white square near the bottom of this image indicates the area scanned in Fig. 5(c), now with the corner of the sensor continuously touching the sample during measurement retracting several microns between scan lines. With pixel spacing reduced to 500 nm and apparent field noise of 0.1 G rms, individual vortices are clearly visible. Fig. 5(d), with 200 nm pixel spacing, resolves the apparent shape of the upper left vortex. On a successive cooldown, after more carefully aligning the sensor to reduce its tilt, single rows of points near a vortex are scanned first along the y, then the x directions, shown in Figs. 5(e) and 5(f).

B. Limits on mechanical aberrations

As depicted in Fig. 5(g), both profiles in Figs. 5(e) and 5(f) are well modeled by the field of an Abrikosov vortex in a YBCO film with known thickness (d=300 nm) and penetration depth (λ=180 nm at 12 K).[20] Because the coherence length is much smaller than the penetration depth, the vortex core is negligible and the London equations govern the field inside the superconductor. The z component of the magnetic field above the film is calculated to be[18]

$$B_z(r,z) = \frac{\Phi_0}{2\pi\lambda^2}\int_0^\infty d\gamma \frac{J_0(\gamma r)e^{-\gamma z}}{\tau[\coth(\tau d/2)+\tau/\gamma]},$$
$$\tau \equiv \sqrt{\gamma^2+\lambda^{-2}}, \tag{1}$$

where Φ_0=20.7 G μm^2 is the magnetic flux quantum and J_0 is the zeroth-order Bessel function of the first kind. $r=\sqrt{(x-x_0)^2+[(y-y_0)A]^2}$ is the radial distance from the center (x_0,y_0) of the vortex; the y axis is scaled by an empirical factor A. z is the height above the top surface of the film. The fit calculates the Hall signal as B_z averaged over the Hall probe's sensitive area, estimated from nominal lithographic

dimensions to be a square 500 nm on a side. The sensor also has a zero-field offset B_{offset}, which is subtracted from the values shown.

Free parameters for the y scan are x_0 and y_0, $A=0.87$, the height of the sensitive area, $h=580$ nm, and $B_{\text{offset}}=-84.0$ G. The Hall coefficient is calibrated to be 0.112 Ω/G. Thus the height and size of the sensitive area are each larger than the penetration depth and are the most important parameters for the apparent size of the vortex.

The sensor is tilted about the x axis by α_x from the horizontal so that only the corner near the sensitive area will come into contact with the flat surface of the sample. α_x is determined optically to be $1.7° \pm 1.0°$. This tilt could add to the measured signal up to 5% of the lateral component of the field, which is insignificant in this model. More importantly, α_x determines h. The corner lies about 10 μm in front of the sensitive area, limited by the accuracy of photolithographic alignment across many sensors fabricated on one chip. Due to this distance and the tilt, the sensitive area is lifted above the surface when the corner rests on the surface. Because of the uncertainty in the tilt, we took h as a free parameter.

The choice of allowing the y-axis scaling to vary as a free parameter is motivated by other images taken with this instrument of lithographically defined structures that show that the y-axis movement of the sensor is smaller than expected from the motor movement and gearing. When the scale is fixed at $A=1$, the residual shows structure symmetric around the vortex center consistent with a scaling error. The physical origin of this disparity between the calculated and actual sensor movements is likely due to position-dependent tilting of the sensor arm. The force exerted on the motion stage by the vacuum and the bellows changes direction as the stage moves along the y axis, rotating the stage and arm slightly.

To first order, this rotation moves the sensor in the y and possibly z directions on top of its intended movement; the x axis is relatively unaffected. The x scan is fitted with the same fixed parameters of the Hall coefficient, sensor dimensions, tilt, and sample penetration depth, but the movement scaling is fixed at the expected value, which did not result in systematic variation in the residual. h is found to be 550 nm and $B_{\text{offset}}=-85.3$ G. The B peak is smaller than in the y scan because the x scan was inadvertently taken 600 nm off the vortex center.

The root mean square of the residuals in Figs. 5(e) and 5(f) is consistent with the 0.11 G rms noise measured in the sensor when it was retracted from the sample and held in a fixed position immediately after the scan (measured with the same bandwidth as when scanning). From this we can place an upper bound of 50 nm rms on the deviation of the sensor position from its expected values within one scan line; less noise or sharper features are required to set a lower bound.

However, Fig. 5(d) shows some evidence that the position repeatability between lines (scanned in the y direction) is not this good. Fitting successive lines separately, the center position of the vortex appears to vary by 200 nm rms, almost all of which must be explained by deviations in the sensor y position between scan lines, rather than by B noise. We also have less systematic evidence of micron-scale position drift over the course of hours when we perform repeated scans of a (presumably stationary) vortex. Such drift plausibly results from thermal expansion of the external stage or other components whose temperatures are not controlled.

These estimates—less than 50 nm rms positional error between points within a line and 200 nm rms error between lines within an image—demonstrate that microstepping and gear reduction can successfully reduce step size, which limited a previous instrument.[9] In our case, the combination of height and size of the Hall probe's sensitive area, rather than any aspect of the stepper motor scanning stage performance, produce the most significant blurring of the features.

Minimizing the sensor tilt about the x axis α_x minimizes the height but is limited by two factors that can prevent the corner near the sensitive area from touching the sample. First, the wire bonds, which protrude downward from the opposite end of the sensor's lower surface, must remain lifted off the sample surface. Second, any inaccuracy in zeroing the tilt about the y axis α_y, together with a small α_x, can lead to one of the side corners of the sensor touching before the tip. Thus the usual alignment procedure entails zeroing α_y visually at room temperature, then imaging vortices at low temperature, modeling the images to determine the height of the sensitive area, and adjusting α_x to minimize this height.

We find that the heights we calculate from vortex images, e.g., $z=580\pm50$ nm, are usually somewhat larger than those we estimate optically from the geometry and tilt of the sensor, $z=300\pm200$ nm. Blurring due to vibrations, not taken into account by the model, may be another factor that appears to increase the calculated height. The amplitude of such vibrations might be up to 60 nm rms, as described in Sec. II F. Dirt on the surface of the sample or the corner of the Hall sensor would also explain the systematic difference. Nonetheless, we expect that improving the sensor fabrication in order to reduce the distance between the Hall cross and the corner, as well as shrink the cross area, will produce the most significant improvement in the instrument's resolution. This effort is in progress.[21]

IV. IMAGING TRANSPORT CURRENTS IN YBCO

To demonstrate the system's applications, we directly image current-induced flux penetration in a YBCO film containing a single artificially induced grain boundary. ac current is applied at ≈400 Hz, as it would be in proposed airborne superconducting generators and motors.[22] We then acquire the series of magnetic images shown in Figs. 6(c)–6(s), each successive image corresponding to a later time in the current cycle. Thus in a realistic context, we can spatially resolve the flux movement and trapping that gives rise to the critical current and ac losses. In the sections below, we first describe the sample, then discuss the features of the magnetic images, leaving the details of the image acquisition to Sec. IV C.

A. YBCO bridge on a bicrystal substrate

The film is grown epitaxially by pulsed laser deposition on a 5° miscut $SrTiO_3$ [001] bicrystal substrate with a

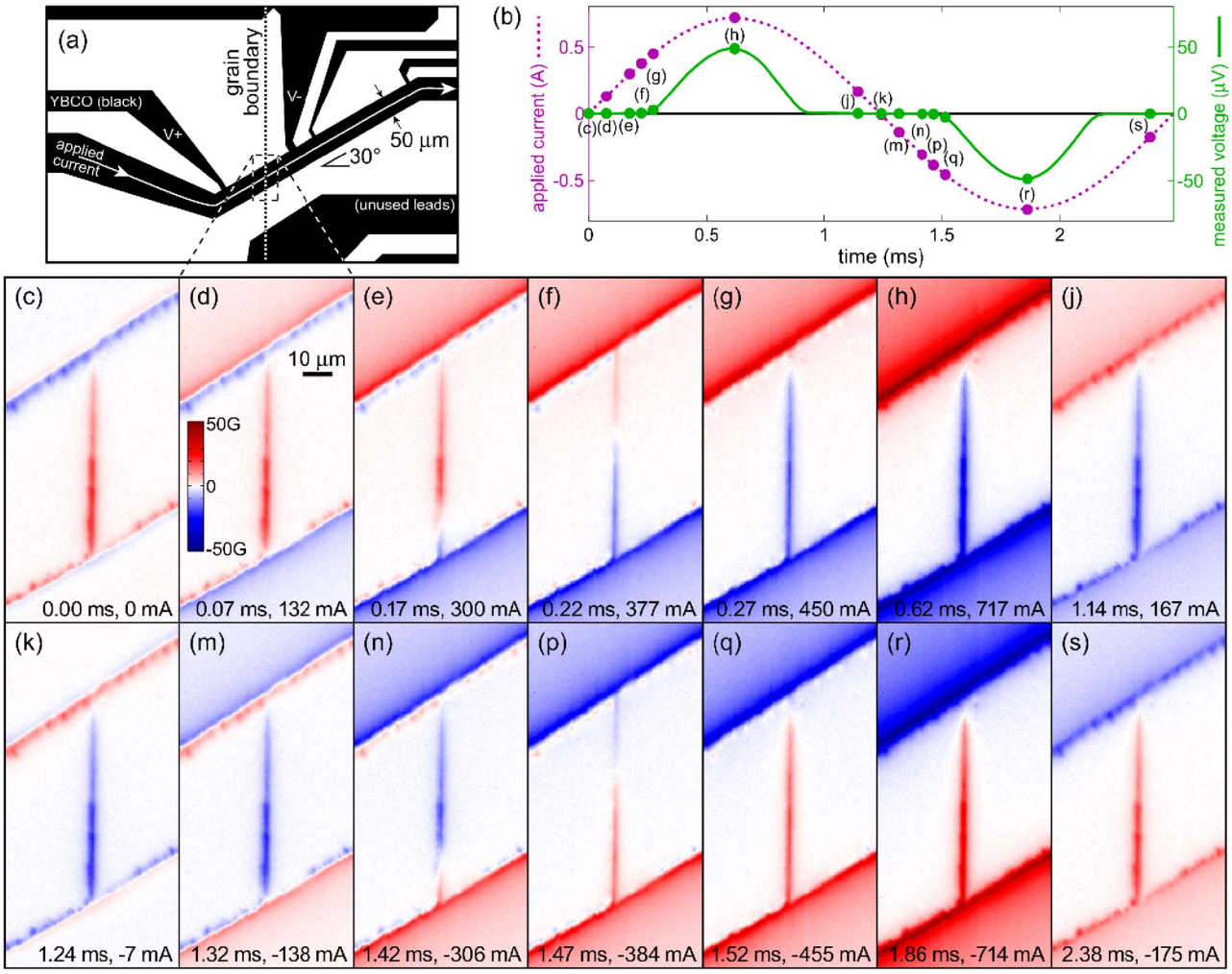

FIG. 6. (Color online) Imaging current-induced flux penetration into a grain boundary: (a)Illustration of the sample geometry. The approximate area of the magnetic images is outlined as a dashed box. A bridge passes current across the boundary while the *V*+ and *V*– leads measure voltage; the other leads are not used. (b) Current (dashed purple line) and voltage (solid green line) during a 500 mA rms, 400 Hz cycle. Select times are marked with labeled dots, and the corresponding magnetic images are shown in (c)–(s). Flux penetrates along the grain boundary well before the bulk of the superconductor admits vortices. The complete set of frames can be downloaded as a movie from Ref. 23.

straight grain boundary. Photolithographic patterning followed by argon-ion milling removes parts of the film leaving a bridge that directs current at 30° relative to the boundary normal, as shown in Fig. 6(a). This is one of the several samples varying the angle between the boundary and the direction of the applied current. The film superconducts below 90 K; it was temperature controlled at 40 K while the Hall sensor was controlled at 54 K.

B. Magnetic imaging results

The series of magnetic images, Figs. 6(c)–6(s), are selected from a larger set to depict the evolution of various features over the ac current cycle emphasizing times at which the field configuration changes qualitatively. The complete set of frames can be downloaded as a movie from Ref. 23. Image (c) shows trapped flux from the previous current cycle along the grain boundary and at various sections near the edge of the bridge. In images (d)–(f), as the applied current increases, vortices of the opposite sign are forced into the boundary from the bottom annihilating the trapped flux as they move upward along the boundary. By image (g), 2.7 μV is measurable across the bridge. Presumably at this point vortices are generating this voltage by continually flowing into the boundary from both ends and annihilating at the point of zero field near the top of the boundary. As the current increases further in image (h), the voltage rises dramatically but must still be due to the grain boundary as most of the strip is still vortex-free. The field does penetrate noticeably along the edges showing some inhomogeneities on a scale of several microns. Decreasing the current to approximately zero in images (j)–(k) leaves the flux trapped as in image (b) but of the opposite sign. The process then repeats showing the opposite fields for negative applied currents over the second half of the cycle.

C. Data acquisition and averaging

The images shown in Figs. 6 and 7 are all derived from one scan. We position the sensor at the first pixel location, measure the ac magnetic response over many current cycles, move to the next pixel, and repeat. We then collate the data corresponding to a particular time relative to the beginning of the current cycle into one image and repeat this for vari-

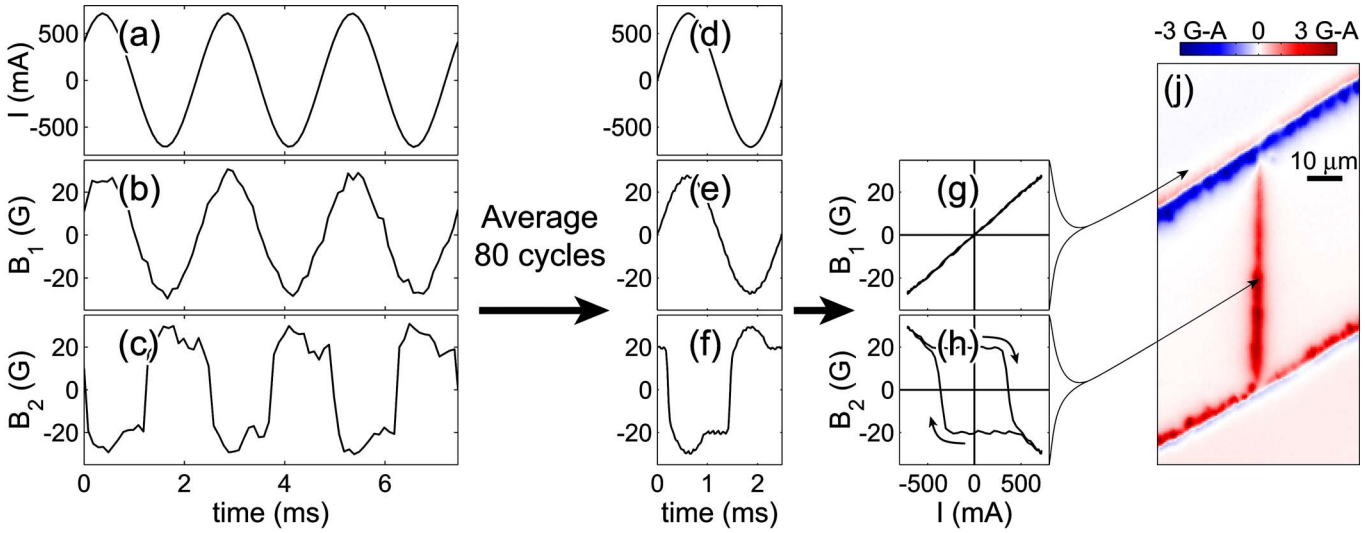

FIG. 7. (Color online) Time traces recorded during imaging of ac current-induced fields. At each pixel, (a) the applied current cycles many times while the magnetic field is recorded. (b) and (c) show the magnetic response at two different pixels. (d)–(f) The cycles are overlaid and averaged. Points from the averaged B wave forms are assembled into the images shown in Figs. 6(c)–6(s) (g), (h) Plotting the averaged current and field against each other yields a hysteresis loop whose area indicates the amount of flux trapping. (b), (e), and (g) correspond to a pixel above the bridge edge where hysteresis is small indicating that a nondissipative Meissner response dominates. In contrast, (c), (f), and (h) are measured at a pixel along the grain boundary where flux is forced in by the applied current and remains after the current is removed leading to a very hysteretic response. The areas of the hysteresis loops for all pixels are assembled in (j) providing a map of ac losses that emphasizes flux penetration along the grain boundary and the bridge edges.

ous times throughout the cycle. Thus the different pixels in one image are not measured simultaneously, and they represent an average magnetic response.

Specifically, we excite the Hall sensor with 24.6 μA dc, connecting its current leads to two 12.6 V lead-acid batteries in series between two 502 kΩ resistors, maintaining the sensor's potential near ground. We apply a continuous, sinusoidal current at 402.7 Hz to the bridge, whose negative contact is grounded. We then raster the sensor over the bridge, pausing at each pixel location to measure the Hall signal for 200 ms. The entire scan takes 4 h.

To record the Hall wave forms, the sensor's voltage leads are connected to differential inputs of a preamplifier (Stanford Research Systems 560) via triaxial cable whose outer shield was grounded to the cryostat. The amplifier output as a function of time t is recorded with 16 bit resolution at 10 kilosamples/s by an analog-to-digital converter (ADC) card (National Instruments AT-MIO-16XE-50) in a personal computer (PC). A separate wave form is taken for each pixel, measured only while the sensor is stationary. The voltages are scaled to magnetic fields $B(t)$ using known sensor and amplifier calibrations. Excerpts of $B(t)$ from two different pixels are shown in Figs. 7(b) and 7(c).

While recording $B(t)$, the ADC card simultaneously records a relatively noiseless wave form proportional to the sample current $I(t)$, as shown in Fig. 7(a), for each pixel.[24] The positive-slope zero-crossing times in $I(t)$ are used to break both I and B into individual current cycles, which are then overlaid and scaled slightly as necessary to make each cycle start and end at the same time.[25] Finally, we averaged these data to obtain the local magnetic response over the cycle as shown in Figs. 7(d)–7(f). The averaging uses a Gaussian window with a full width at half maximum (FWHM) of 25 μs evaluated every 25 μs over the 2.5 ms period.

The choice of a 25 μs time step is based on the settling time of the ADC.[26] A given sample actually represents an average of the signal over a fraction of this time interval, limiting the rate at which any feature will appear to change. With improved electronics, however, the technique described here could be used to image much faster periodic phenomena.

The averaging constitutes a software lock-in technique that suppresses components of the signal that are not periodic in the frequency of the applied current. For instance, the field of a single vortex moving by a pixel would be largely averaged out, unless its position is reproducible from cycle to cycle. We also discard the mean of the averaged $B(t)$ at each pixel, isolating the response to the sample current from any static ambient field or slowly varying Hall voltage offset. Finally, the data from all pixels are assembled into 100 images corresponding to 25 μs time slices.

The same process of breaking into cycles and averaging is applied to the sample voltage V. After the magnetic scan, simultaneous $I(t)$ and $V(t)$ are recorded at 10 kilosamples/s for 100 s. The average I and V over the cycle are plotted in Fig. 6(b).

A standard lock-in measurement—multiplying $B(t)$ by $I(t)$ and measuring the dc component of the result—would yield the strength of the first harmonic in the B wave form, which would correctly represent the data if $B(I)$ were always linear as in Fig. 7(g). This is approximately true in the Meissner regime i.e. when the applied current is too small for vortices to penetrate. In contrast vortex movement causes a nonlinear hysteretic $B(I)$ as in Fig. 7(h)—higher harmonics of the driving frequency make up a significant part of the signal. In this case the data is better visualized as the series of images in Figure 6(c)–6(s), where each frame is a compilation of B from all pixels at the same time in the current

cycle, assembled from the interpolated wave forms $B(t')$.

Interpretation of these images is clarified by scans of a similar sample, not shown—a bridge perpendicular to a grain boundary. Two scans were taken in succession applying current of the same amplitude but different frequencies: 400 Hz vs 40 Hz. The scans show no statistically significant difference except for a 2 μm shift in spatial position. Thus we believe that each of Figs. 6(c)–6(s) is a quasistable field configuration $B(I)$ over its 25 μs interval, insensitive to the rate at which the current is swept.

Figure 7(j) compiles the areas of the B-I hysteresis loops, $\int_{I_{\min}}^{I_{\max}}[B_{\uparrow}(I)-B_{\downarrow}(I)]dI$, where $B_{\uparrow}$ is the magnetic field on the branch of the loop where the current is increasing and $B_{\downarrow}$ the reverse. This "dissipation map" is a compact way to identify regions of flux trapping that cause hysteretic ac loss. As in Figs. 6(c)–6(s), the grain boundary and patches along the bridge edges stand out.

V. POSSIBLE DESIGN PERMUTATIONS

A. Other scanned probes including scanning SQUID

Other probes with unique advantages could be substituted for the Hall sensor. For example, studies of dissipation in superconductors would benefit from electric potential imaging, which could be achieved with a conducting tip. The tip could even be integrated into a Hall sensor for correlated electric and magnetic measurements.

A SQUID could be substituted for its superior field sensitivity, $\approx 10^{-7}$ G/$\sqrt{\text{Hz}}$, albeit at some cost in spatial resolution, 10 μm.[5] An important consideration for using a SQUID in our instrument is temperature control. The SQUID must be held below its critical temperature; in the present configuration, the sensor arm is cooled via the sample stage and cannot be maintained colder than the sample. Thus the sample would have to remain below about 9 K for a niobium SQUID or 90 K for a high-T_c SQUID. To circumvent this restriction, we could place the SQUID on the sample stage and scan the sample using the arm. A niobium SQUID has been used successfully in a similar configuration with sample temperatures up to 150 K.[27] The SQUID could be mounted on a bracket that holds it above the sample with the sample facing up so as not to obscure optical alignment of the sensor to sample features.

B. Applied magnetic field

The system does not have a built-in magnet for applying a field to the sample. Desert Cryogenics incorporates superconducting, solenoidal magnets into similar cryostats achieving 1 T with $\approx$60 A applied current. The liquid-helium flow is split to cool the magnet and sample stage separately.

For fields below about 0.1 T, nonsuperconducting coils could be placed outside the cryostat. An iron flux guide that wraps around the cryostat would enhance the coils's field by providing a high-permeability return for the flux. The flux guide also allows more flexible placement of the coils. Furthermore, the guide can terminate in pole pieces brought close to the sample and shaped to further concentrate the field while maintaining field homogeneity at the sample.[28]

C. Motion stage improvements

Temperature controlling the positioning stage might eliminate the 2 μm drift observed between successive images taken at nominally identical positions. It may also reduce deviations in the y-axis positions between scan lines. The stage would be maintained slightly above room temperature via a thermally insulating enclosure, thermocouples, resistive heaters, and feedback electronics.

Our current design, in which the positioning stage is external to the vacuum chamber, has the advantage that the motors, gears, screws, and associated lubricants need not be vacuum compatible. Vacuum-compatible substitutes are, however, commercially available.[29] If the stage were inside an extension of the vacuum chamber, it would not need to overcome the forces of atmospheric pressure and bending bellows. The y range would improve and the y-axis scaling, discussed in Sec. III B, would likely be eliminated. More generally, reduced torque on the stage would mean less disparity between movements of the stage and movements of the end of the sensor arm. Adding optical linear position encoders for closed-loop positioning would likely be more effective than in the current configuration.

In vacuum but at room temperature and in the absence of large forces, piezo-based actuators could substitute for the stepper motors. Piezos can generate long range motion through a series of short steps. Implementations include "stick-slip" (inertial) motion[30] and "inchworm" behavior.[31] Typically the step size is not repeatable enough to be used directly for scanning, but optical linear encoders allow closed-loop positioning with 20 nm accuracy, which would be suitable for SHPM.

Temperature drift of the stage in vacuum (even with some contact to a base) would be larger in the absence of temperature feedback, but once implemented, feedback would be more precise.

ACKNOWLEDGMENTS

The Hall sensors were fabricated by Janice Wynn Guikema using GaAs/AlGaAs heterostructures grown by David Kisker. The YBCO films in Sec. II A, III, and IV, were grown by Jeong-uk Huh at Stanford, Luke Peng at Superconductor Technology, Inc., and George Daniels and Matt Feldmann at the University of Wisconsin—Madison. Eric Hung helped with initial construction of the instrument. Ophir Auslaender took the SEM of the Hall sensor tip. This work is supported by the Air Force Office of Scientific Research and the Air Force Multi-University Research Initiative (MURI).

[1] A. M. Chang *et al.*, Appl. Phys. Lett. **61**, 1974 (1992).
[2] S. J. Bending, Adv. Phys. **48**, 449 (1999).
[3] A. Tonomura, T. Matsuda, H. Tanabe, N. Osakabe, J. Endo, A. Fukuhara, K. Shinagawa, and H. Fujiwara, Phys. Rev. B **25**, 6799 (1982).
[4] M. R. Koblischka and R. L. Wijngaarden, Supercond. Sci. Technol. **8**, 199 (1995).
[5] J. R. Kirtley, M. B. Ketchen, K. G. Stawiasz, J. Z. Sun, W. J. Gallagher, S. H. Blanton, and S. J. Wind, Appl. Phys. Lett. **66**, 1138 (1995).
[6] Y. Martin and H. Wickramasinghe, Appl. Phys. Lett. **50**, 1455 (1987).
[7] J. Siegel, J. Witt, N. Venturi, and S. Field, Rev. Sci. Instrum. **66**, 2520 (1995).
[8] A. Sandhu, H. Masuda, H. Senoguchi, and K. Togawa, Nanotechnology **15**, S410 (2004).

[9] J. K. Gregory, S. J. Bending, and A. Sandhu, Rev. Sci. Instrum. **73**, 3515 (2002).
[10] D. Larbalestier, A. Gurevich, D. M. Feldmann, and A. Polyanskii, Nature (London) **414**, 368 (2001).
[11] Desert Cryogenics is now a division of Lake Shore Cryotronics, Inc., http://www.lakeshore.com
[12] E. Zeldov, J. R. Clem, M. McElfresh, and M. Darwin, Phys. Rev. B **49**, 9802 (1994).
[13] A. K. Geim, S. V. Dubonos, J. G. S. Lok, I. V. Grigorieva, J. C. Maan, L. T. Hansen, and P. E. Lindelof, Appl. Phys. Lett. **71**, 2379 (1997).
[14] J. Guikema, Ph.D. thesis, Stanford University, 2004.
[15] The pump was an XDS5 dry scroll pump manufactured by BOC Edwards, http://www.bocedwards.com
[16] Two positions with large gradients in the Hall voltage in different directions were examined. At the first, dV/dx was −85, dV/dy was −45, and dV/dz was −33 μV/μm. At the second, dV/dx was −39, dV/dy was 34, and dV/dz, −1.2 μV/μm. These gradients may have been due to an electrical interaction between the sample and sensor, rather than magnetic vortices. They were, however, approximately constant over a 600 nm diameter and reproducible between scans before and after the vibration measurement.
[17] J. Pearl, J. Appl. Phys. **37**, 4139 (1966).
[18] A. M. Chang, H. D. Hallen, H. F. Hess, H. L. Kao, J. Kwo, A. Sudbo, and T. Y. Chang, Europhys. Lett. **20**, 645 (1992).
[19] G. Carneiro and E. H. Brandt, Phys. Rev. B **61**, 6370 (2000).
[20] S. Djordjevic, E. Farber, G. Deutscher, N. Bontemps, O. Durand, and J. Contour, Eur. Phys. J. B **25**, 407 (2002).
[21] C. W. Hicks, M. A. Topinka, J. H. Bluhm, J. Guikema, E. Zeldov, H. Shtrikman, and K. A. Moler, American Physical Society March Meeting, March 24, 2005, Los Angeles, CA (unpublished).
[22] S. Kalsi, Proc. IEEE **92**, 1688 (2004).
[23] See EPAPS Document No. E-RSINAK-76-212510 for the complete set of grain boundary images assembled into a movie. This document can be reached through a direct link in the online articles's HTML reference section or via the EPAPS homepage (http://www.aip.org/pubservs/epaps.html).
[24] The ADC card actually acquires the two wave forms by scanning its ADC between the two inputs, thus the samples are interleaved in time rather than simultaneous. The resultant 50 μs time shift is corrected before averaging the Hall or sample voltage wave forms.
[25] Instead of finding zero crossings, one could fit a sinusoid to $I(t)$ to determine its frequency and phase, which could be used to break $B(t)$ into cycles. We found, however, that $I(t)$ showed slight, but statistically significant, variations in frequency within each wave form causing the sinusoid to misrepresent some cycles.
[26] The ADC card is rated to settle from full range to 1 least-significant bit within 50 μs. In the 25 μs interval used here, it would settle to 4 mV, which translates to a magnetic field of 0.1 G, from the maximum value of 1 V.
[27] J. R. Kirtley, C. C. Tsuei, and K. A. Moler, Science **285**, 1373 (1999).
[28] Such a magnet was designed and built into a Desert Cryogenics probe station by Dr. Douwe Monsma in Professor Charles Marcus's laboratory at Harvard University.
[29] See, for example, vacuum-compatible stepper motors from tectra GmbH Physikalische Instrumente, http://www.tectra.de, or servo motors from Aerotech, Inc., http://www.aerotech.com
[30] For example, Physik Instrumente (PI) GmbH & Co. KG, http://www.pi.ws, makes closed-loop, stick-slip piezo actuators.
[31] See EXFO Burleigh Products Group Inc.'s Inchworm® motors, http://www.exfo.com, or Bookham Inc. New Focus division's Picomotors™, http://www.newfocus.com